INTERNATIONAL JOURNAL FOR NUMERICAL METHODS IN BIOMEDICAL ENGINEERING
Int. J. Numer. Meth. Biomed. Engng. (2015); e02706
Published online in Wiley Online Library (wileyonlinelibrary.com). DOI: 10.1002/cnm.2706

Processing the image gradient field using a topographic primal sketch approach

A. M. Gambaruto*,†

Computer Applications in Science & Engineering (CASE), Barcelona Supercomputing Center, Nexus I – Campus Nord UPC, C/ Jordi Girona 2, 08034, Barcelona, Spain

SUMMARY

The spatial derivatives of the image intensity provide topographic information that may be used to identify and segment objects. The accurate computation of the derivatives is often hampered in medical images by the presence of noise and a limited resolution. This paper focuses on accurate computation of spatial derivatives and their subsequent use to process an image gradient field directly, from which an image with improved characteristics can be reconstructed. The improvements include noise reduction, contrast enhancement, thinning object contours and the preservation of edges.

Processing the gradient field directly instead of the image is shown to have numerous benefits. The approach is developed such that the steps are modular, allowing the overall method to be improved and possibly tailored to different applications. As presented, the approach relies on a topographic representation and primal sketch of an image.

Comparisons with existing image processing methods on a synthetic image and different medical images show improved results and accuracy in segmentation. Here, the focus is on objects with low spatial resolution, which is often the case in medical images. The methods developed show the importance of improved accuracy in derivative calculation and the potential in processing the image gradient field directly.

Received 29 June 2014; Revised 14 January 2015; Accepted 26 January 2015

KEY WORDS: finite difference least squares; contrast enhancement; image filtering; segmentation, reconstruction from gradient field

1. INTRODUCTION

Image processing of medical data is an active and diverse field of research. The focus is ameliorating images acquired from scans to facilitate the tasks of identifying, analysing and describing desired features. These tasks are typically very specific depending on the clinical need; however, the variety of tools and procedures used is, broadly speaking, often common to different scenarios and can include denoising, contrast enhancement, restoration and bias correction, amongst others. Successful algorithms improve visual quality; however, the aim is usually geared towards robustness and accuracy of object identification and segmentation. Review articles with reference to different topics and applications to medical images can be found in [1–5].

Despite the broad spectrum of goals, most methods make direct use of the image intensity scalar field. Some examples popular in the image processing community include median filter and non-local means [6] for denoising; and unsharp masking [7], difference of Gaussians [8], multi-scale retinex [9–11] and automatic colour equalisation [12] for contrast enhancement. Several methods use a frequency representation of the image intensity, while other methods seek use of spatial derivatives such as the anisotropic filters [13–16]. Some methods have been proposed to quantify the

*Correspondence to: A. M. Gambaruto, Computer Applications in Science & Engineering (CASE), Barcelona Supercomputing Center, Nexus I – Campus Nord UPC, C/ Jordi Girona 2, 08034 Barcelona, Spain.
†E-mail: alberto.gambaruto@bsc.es

effectiveness of the image processing using reduced measures [4, 17, 18]; however, they remain general and do not address adequately interests of the medical field.

Another approach is to process the image gradient field and subsequently reconstruct an image from it. Some promising preliminary results of this procedure have been reported in [19]. In the current work, this approach is developed to improve the accuracy of the computations, as well as introducing a flexible and modular set of processing steps, which can be readily tailored to different targeted applications.

Here, the focus will be on medical image processing for object segmentation, with special interest in cases of poor available spatial resolution. The proposed method uses a topographic primal sketch [20] interpretation of the image, identifying distinct attributes to be processed to attain (i) careful preservation of object boundaries; (ii) a more direct way of enhancing object contrasts; and (iii) a simplified identification and removal of noise. After the image gradient field has been processed, the image is reconstructed through a process of integration that smoothly approximates the gradient field.

In order to process the gradient field of an image, it is necessary to compute the spatial gradients accurately. This task is not trivial, especially in the case of limited resolution and the presence of noise. Computing derivatives on gridded data often relies on using a finite difference (FD) approach; however, this can be sensitive to noise, and the use of the Sobel operator is known to be a better approach as it performs a local average. The convolution of the image with the derivative of a Gaussian function is a popular approach and is based on the notion of scale space (SS) [13, 21, 22]. Another approach involves fitting a polynomial function to the image intensity [23, 24], which has been popular because of the good low-pass properties as a filter [25, 26]. Here, this last method is adapted to include outliers and is recast as a least squares (LS) fit to a Taylor series [27, 28], showing improved accuracy over the other approaches.

The paper is divided in the following sections. The test images are first presented in Section 2. Section 3 is dedicated to presenting and comparing methods for calculating the spatial derivatives: existing methods are briefly outlined, while more detail is provided for the novel LS approach. An overview of filtering methods is then given in Section 4 in order to provide a context to subsequent performance assessments. The methods for processing the image gradient field and the subsequent reconstruction of an image are given in Section 5. The results and comparison of methodologies are given in the results Section 6 and discussed in Section 7. Finally, the conclusions are presented in Section 8.

2. TEST IMAGES USED

The images used in this work comprise of a small selection, shown in Figures 1 and 2, and are chosen to highlight features of the analysis and provide a varied test set:

- synthetic image generated using the arctangent function (*arctan image*): contains an edge of varying steepness, ideal for studying how the processing methods handle the delineation of objects;
- high-speed photograph from confocal microscopy experiments of red blood cells [29] (*microscopy image*): contains loss of contrast due to cells not lying perfectly on the focal plane;
- computed tomography angiography (CTA) of the lower abdomen, specifically the descending aorta at the aorto-iliac bifurcation (*abdominal CTA image*): the image contains several objects of varying dimensions, image acquisition resolution $(0.7773 \times 0.7773 \times 1)$ mm;
- axially acquired computed tomography (CT) of the cranium but visualised in the coronal plane to identify the nasal cavity as is often the case when studying the respiratory airways [30] (*cranial CT image*): the thin scroll-like structure suffers from inadequate resolution, image acquisition resolution $(0.5059 \times 0.5059 \times 1)$ mm.

Both CT scans were requested for clinical reasons, and consent from the patient for subsequent use of the data was obtained. The experimental work with red blood cells has been approved by an ethics committee. The images acquired were part of a sequence (spatial or temporal); however,

DOI: 10.1002/cnm

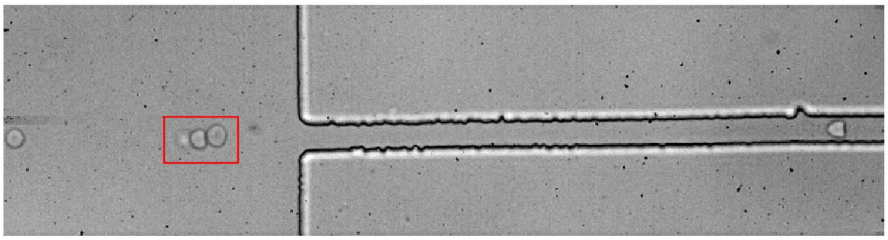

'*microscopy image*': confocal microscopy image of red blood cells motion in a micro-channel

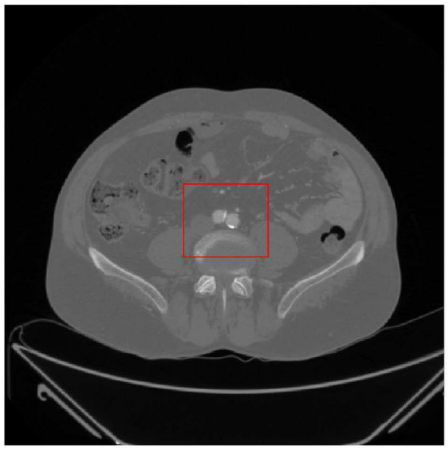

'*abdominal CTA image*': axial CTA of the lower abdomen at a section of the aorto-iliac bifurcation

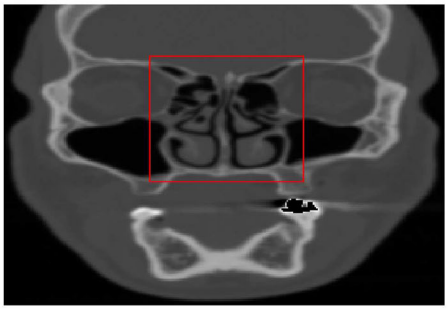

'*cranial CT image*': coronal projection of a CT stack of images to identify the nasal cavity

Figure 1. Medical images used for testing the image processing methods. The pixel resolution is normalised; hence, the voxel size is $(1 \times 1 \times 1)$. Regions of interest are identified.

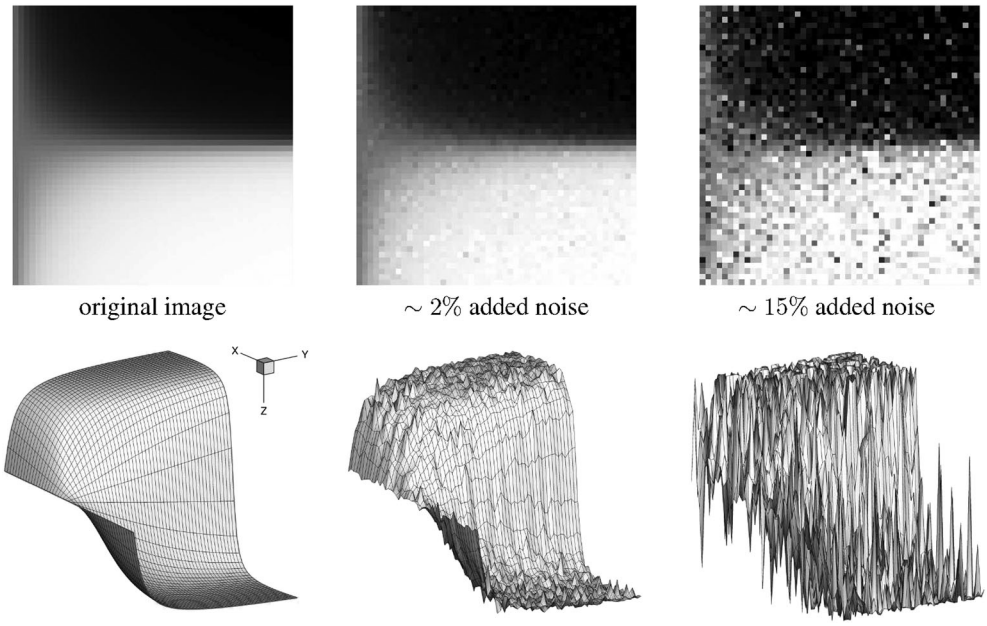

Figure 2. Synthetic image of the arctangent function (equations (1)–(2)), without noise and with noise (∼2% and ∼15% of the signal amplitude). Top row: scaled image; bottom row: visualisation as topographic landscape.

DOI: 10.1002/cnm

in this work, only the individual two-dimensional images are considered, inferring no information from the sequence. Furthermore, no consideration of texture is used in this work.

The medical images are cropped to focus in detail on desired features and facilitate the presentation of results. It is evident that small portions of these images hold the desired objects (at a given instance in the image stack), resulting in poor effective resolution. Noise and imaging artefacts will have a greater influence because of this poor spatial sampling, introducing more uncertainty in the perception of the image. Prior to any processing, the images must be interpreted to extract all relevant information, and all subsequent treatment of the images must then ensure that this information is preserved. In this work, the underlying image information is presented as a topographic primal sketch [20].

The cropped images are padded by pixels with mirror values, hence obtaining a zero gradient across the boundary. The images are scalar-valued, hence a grey-scale, and the intensities are normalised to $[0, 255]$. In this paper, note that all figures (including the figures of image gradients) are scaled to this range to improve visibility. The resulting images are considered as matrices $I(x, y)$ of dimension $(1, n_x) \times (1, n_y)$; hence, the x-axis is aligned to the row index and the y-axis to the column index.

The synthetic *arctan image* is given by

$$f(x, y) = \arctan(10x(1 + y)) \qquad x = [-1, 1]\,;\ y = [-1, 1] \tag{1}$$

and then scaled to the range $[0, 255]$, and parametrised on a 50×50 sample grid, as shown in Figure 2. This test function is used as it contains a line of varying gradient magnitude, aligned with an axis direction, and approximately plateau regions on either side. These properties can be used to study features of image processing very simply, such as the identification of object contours and effects of noise.

Noise is added to this synthetic image after it has been scaled, by following the approach presented in [15] for generating speckle-like noise. Two noisy matrices of the same dimension of the image are produced, I_{rand1} and I_{rand2}, having standard normal distribution (mean$=$ 0 and standard deviation$=$ 1) and scaled by γ. The Hadamard product (pointwise product) of these matrices is then taken to produce the noisy image

$$I_{noisy} = I + \gamma \cdot I_{rand1} \circ I_{rand2} \tag{2}$$

where $\circ$ denotes the Hadamard product. The PDF of such noise has enhanced large and small deviations compared with the normal distribution. The noisy image is then saturated, such that any pixel with an intensity greater than 255 or less than 0, due to the addition of the noise, is truncated to the respective limits. Two values of $\gamma = 5$ and $\gamma = 40$ are tested, representing $\sim$2% and $\sim$15% of the signal amplitude, respectively. The maximum absolute differences between noisy and original images are $\sim$12% and $\sim$77%, respectively. The effect of noise on the function is shown in Figure 2.

3. CALCULATING SPATIAL DERIVATIVES ACCURATELY

The computation of the image intensity spatial derivatives is an important component of many image processing methods and is often used to identify object contours or as part of anisotropic filtering methods. In this work, the accuracy and robustness of calculating gradients are of specific interest as the image processing is to be performed directly on the gradient field. As such, a selection of methods for computing the spatial derivatives is compared. A novel approach is derived in the following, while some popular approaches are briefly presented in the Appendix and listed here. For brevity of notation, we write $\nabla I(x, y) = [I_x(x, y), I_y(x, y)]^T$.

- Finite difference (FD): the second-order centred scheme;
- Sobel operator ($Sobel$): same as FD method, with additional smoothing by local averaging;
- Scale space (SS): relies on taking the derivatives of the image at a certain scale σ. This is computed as $\nabla I_\sigma = \nabla (I \otimes G_\sigma) = I \otimes \nabla G_\sigma$, where G is a Gaussian and $\otimes$ denotes convolution. The spatial derivatives calculated with method will be denoted by 'SS_σ^m' for brevity, where σ is the standard deviation of the Gaussian function and m is the mask size. For example, SS_1^5

DOI: 10.1002/cnm

indicates a use of $\sigma = 1$ and a mask size of 5×5. In this work, two configurations are used for comparative purposes: $SS^3_{0.5}$ and SS^5_1. These two configurations are chosen to keep σ small to avoid excessive blurring, and the mask size is sufficiently large to capture the variation in Gaussian weights. Similar parameters are commonly chosen [31, 32]

- Savitzky–Golay (SG): the image is approximated using a polynomial function (monomial basis), through an LS procedure [23–25, 33–36]. The spatial derivatives calculated with this method will be denoted by '$\mathrm{SG}^{m,o}_d$' for brevity, where d is the order of the polynomial function, m is the mask size and o is the number of outliers considered.

3.1. Least squares approximation to a Taylor series

We now develop a final approach to obtain spatial derivatives of the image intensity that has attracted interest in the meshless FD community [27, 28, 37, 38] and is closely related to the SG method as will be discussed later. The possibility of estimating outliers is developed, and this is shown to improve the accuracy of the computations. The method works by applying an LS minimisation to the terms in the Taylor expansion, and the following derivation is based on the work of [27, 37].

For any sufficiently differentiable function $f(x, y)$ in a given domain, the Taylor series expansion around a point $\mathbf{x}_0 = (x_0, y_0)$ can be used:

$$\begin{aligned} f =& f_0 + \Delta x \frac{\partial f_0}{\partial x} + \Delta y \frac{\partial f_0}{\partial y} \\ &+ \frac{1}{2!}\left[\Delta x^2 \frac{\partial^2 f_0}{\partial x^2} + \Delta y^2 \frac{\partial^2 f_0}{\partial y^2} + 2\Delta x \Delta y \frac{\partial^2 f_0}{\partial x \partial y}\right] \\ &+ \frac{1}{3!}\left[\Delta x^3 \frac{\partial^3 f_0}{\partial x^3} + \Delta y^3 \frac{\partial^3 f_0}{\partial y^3} + 3\left(\Delta x^2 \Delta y \frac{\partial^3 f_0}{\partial x^2 \partial y} + \Delta y^2 \Delta x \frac{\partial^3 f_0}{\partial y^2 \partial x}\right)\right] \\ &+ O(\epsilon^4) \end{aligned} \tag{3}$$

where $f = f(x, y)$, $f_0 = f(x_0, y_0)$, $\Delta x = x - x_0$, $\Delta y = y - y_0$, $\epsilon = \sqrt{\Delta x^2 + \Delta y^2}$. Truncating the expansion to second-order terms (for ease of readability), for a given point pair, we can write the expansion as

$$s_i^T \, \delta f = f_i - f_0 \tag{4}$$

where

$$s_i^T = \left(\Delta x_i, \Delta y_i, \Delta x_i^2/2, \Delta y_i^2/2, \Delta x_i \Delta y_i\right) \tag{5}$$

and the unknown derivatives at point x_0, y_0 are

$$\{\delta f\}^T = \left(\frac{\partial f_0}{\partial x}, \frac{\partial f_0}{\partial y}, \frac{\partial^2 f_0}{\partial x^2}, \frac{\partial^2 f_0}{\partial y^2}, \frac{\partial^2 f_0}{\partial x \partial y}\right) \tag{6}$$

If we consider n neighbouring points and stack s_i^T for $i = 1, \ldots, n$, this can be rewritten as a linear system:

$$[S]\{\delta f\} - \{f\} = 0 \tag{7}$$

or explicitly

$$[S] = \begin{pmatrix} \Delta x_1 & \Delta y_1 & \Delta x_1^2/2 & \Delta y_1^2/2 & \Delta x_1 \Delta y_1 \\ \Delta x_2 & \Delta y_2 & \Delta x_2^2/2 & \Delta y_2^2/2 & \Delta x_2 \Delta y_2 \\ \vdots & \vdots & \vdots & \vdots & \vdots \\ \Delta x_n & \Delta y_n & \Delta x_n^2/2 & \Delta y_n^2/2 & \Delta x_n \Delta y_n \end{pmatrix} \quad ; \quad \{f\} = \begin{pmatrix} f_1 - f_0 \\ f_2 - f_0 \\ \vdots \\ f_n - f_0 \end{pmatrix} \tag{8}$$

DOI: 10.1002/cnm

Note that in the general case, by fixing a compact support radius (or alternatively a mask size), the system is overdetermined. In the above example, there are five unknowns (equation (6)); while using a 3×3 mask size, we find the dimensions of matrix S to be 8×5. An LS fit is employed to minimise the error functional $\sum_{i=1}^{n} |[S]\{\delta f\} - \{f\}|^2$. The derivatives are given by the Moore–Penrose pseudo-inverse as

$$\delta f = \left(S^T S\right)^{-1} \left(S^T f\right) \tag{9}$$

where matrix $S^T S$ is square, symmetric and positive semi-definite.

It is important to note that by considering $\{f\} = \{f_i - f_0\}$, the LS fit is performed only on the image derivatives and not the intensity values [28]. This is an important difference with respect to the SG class of methods [23–25], which approximates the image intensity values (low-pass filter), and hence loses the interpolation property of equation (4). Furthermore, we note that the equivalent matrix $S^T S$ for the SG method is one dimension bigger and will lead to a marginal increase in computational time, especially if this procedure is repeated for each pixel.

As derived so far, each point in the neighbourhood for $\mathbf{x_0}$ has equal importance, and the error is evenly distributed. However, we would like to evaluate the derivatives at $\mathbf{x_0}$, and hence, it is important to weight errors accordingly: to be more accurate closer to $\mathbf{x_0}$ and tolerate larger errors at pixels further away. Several weighting functions are proposed in the literature [37, 38]; however, for simplicity, we will use $w = 1/r$, where r is the distance between the pixel pair considered. For the linear system, the weights can be assembled into a diagonal matrix W. Putting everything together, we obtain

$$\delta f = \left[\left(S^T W S\right)^{-1} S^T W\right] f \tag{10}$$

The matrix system need only be computed once for a given mask size and expansion order, if no outlier is considered.

To obtain estimates of higher-order derivatives and better accuracy of low-order terms when no noise is present in the image, higher orders for the Taylor expansion can be considered. For example, if using fourth-order accuracy in the Taylor expansion, then with this LS approach, we will obtain third-order accuracy in the first-order derivatives, and second-order accuracy in the second-order derivatives [37]. An alternative approach to obtain higher-order terms is to repeat a lower-order expansion on previously calculated lower derivatives [39]; however, this approach is not employed in this work.

The method can be extended to exclude outliers in the data set. A simple approach to identify outliers is to first calculate an initial estimate of $\nabla I(x, y)$ using equation (10) and subsequently compare the result obtained with another approach for estimating the gradient for each pixel in the data set:

$$\nabla I_{ij} = \frac{(I_j - I_i)(\mathbf{x}_j - \mathbf{x}_i)}{|\mathbf{x}_j - \mathbf{x}_i|^2} \qquad \text{for } j = 1, n \tag{11}$$

where i denotes the reference pixel, j is the neighbouring pixel, n is the total number of neighbouring pixels in the set and $\mathbf{x} = [x\ y]^T$ is the coordinate of the pixel in the Cartesian frame. The outliers are defined as those with largest error $|\nabla I_i - \nabla I_{ij}|$. Having identified and excluded the desired number of outliers from the set, the above LS procedure (equation (10)) will be repeated to obtain a more accurate derivative approximation. In this way, matrix S will vary, and equation (10) must be computed for each pixel. Note that an alternative for identifying outliers would be to select the largest residual (misfit) from equation (7).

The spatial derivatives calculated with this method will be denoted by '$\mathrm{LS}_d^{m,o}$' for brevity, where d is the order of the Taylor expansion, m is the mask size and o is the number of outliers considered (note: if not specified $o = 0$ is inferred). For example, LS_4^5 indicates a use of a Taylor expansion to include fourth-order terms and a mask size of 5×5, with no outliers considered.

DOI: 10.1002/cnm

3.2. Comparison of spatial derivative methods

The different approaches for calculating the spatial derivatives of the image intensity are now compared. These approaches are FD, Sobel, SS, SG and Taylor series LS. Equations for these methods are found in the Appendix, while the LS method is given by equation (10). In order to quantify the accuracy, we first observe results on the *arctan image*. In Table I, the error between the analytic function and discrete approximations is given, averaged over the entire image, ϵ_{img}, or over two sections, ϵ_{L1} and ϵ_{L2}, that have a shallow and steep gradient, respectively. The error has been normalised to the smallest gradient magnitude of the analytic image when comparing the no-noise case and to the largest gradient magnitude when comparing the noise-corrupted cases.

We summarise the table with a few key results. When the image has no noise, all methods perform well except for $|\nabla I|_{SS_1^5}$, while $|\nabla I|_{LS_4^5}$ is the most accurate. In the presence of noise, $|\nabla I|_{LS_2^5}$ performs best; however, in cases where we wish to avoid larger mask sizes because of possible poor image resolution, we note that $|\nabla I|_{LS_2^{3,1}}$ performs well. When the image is corrupted by noise, the FD approach $|\nabla I|_{FD}$ yields poor results, as does the high-order LS $|\nabla I|_{LS_4^5}$. The poor performance of $|\nabla I|_{LS_4^5}$ with noise is caused by the method not being able to discard the effect of noise, which can be achieved by using a greater mask size (hence more redundancy given by a more overdetermined system) or the identification of outliers. For small mask sizes, we note that $|\nabla I|_{Sobel}$ outperforms $|\nabla I|_{SS_{0.5}^3}$.

An important point to note is that for corresponding mask sizes, the LS $|\nabla I|_{LS}$ results are superior, and the use of an outlier greatly improves the results from $|\nabla I|_{LS_2^3}$ to $|\nabla I|_{LS_2^{3,1}}$, for example. Finally, we observe a small increased accuracy in $|\nabla I|_{LS_2^{3,1}}$ compared with $|\nabla I|_{SG_2^{3,1}}$.

The results of calculating the gradient magnitude for the synthetic *arctan image* are shown in Figure 3. Visually, we can appreciate the accuracy of the results. We note that the methods with larger mask sizes tend to blur the gradient field, which not only reduces the effect of noise but also results in possibly unnecessary loss of accuracy. Comparing approaches $|\nabla I|_{LS_2^{3,1}}$ and $|\nabla I|_{SS_1^5}$, we note that the results are better on the whole for $|\nabla I|_{LS_2^{3,1}}$, despite having a smaller mask size. This points to an important improvement in accuracy in the presence of noise by using the LS approach and allows for its use in cases of limited resolution by being able to use a smaller mask size.

Table I. Mean absolute percentage error in calculating the derivatives in the *arctan image* with respect to the analytic solution.

		I (no noise)			I_{noise} (∼2% noise)			I_{noise} (∼15% noise)		
		ϵ_{img}	ϵ_{L1}	ϵ_{L2}	ϵ_{img}	ϵ_{L1}	ϵ_{L2}	ϵ_{img}	ϵ_{L1}	ϵ_{L2}
3 × 3 mask	$\|\nabla I\|_{FD}$	**85**	**15**	**164**	6.8	9.7	6.8	43	43	31
	$\|\nabla I\|_{Sobel}$	87	19	165	4.3	6.0	4.4	27	29	20
	$\|\nabla I\|_{SS_{0.5}^3}$	**85**	16	**164**	5.5	7.8	5.4	35	36	24
	$\|\nabla I\|_{LS_2^3}$	88	21	165	4.1	5.6	4.3	26	28	19
	$\|\nabla I\|_{LS_2^{3,1}}$	88	20	165	**3.9**	**4.4**	**3.5**	**20**	**19**	**17**
	$\|\nabla I\|_{SG_2^{3,1}}$	88	21	165	4.0	4.8	4.0	21	**19**	18
5 × 5 mask	$\|\nabla I\|_{SS_1^5}$	954	986	903	4.6	5.6	4.7	19	19	14
	$\|\nabla I\|_{LS_2^5}$	235	62	420	*1.9*	*1.7*	*2.2*	*10*	*9*	*8*
	$\|\nabla I\|_{LS_4^5}$	*23*	*1*	*52*	4.8	7.1	5.2	31	31	23

Results for 'I (no noise)' are normalised to $\min(|\nabla I|_{analytic})$, while for the noisy image, the normalisation is $\max(|\nabla I|_{analytic})$. First column ϵ_{img}: average over the entire image; second column ϵ_{L1}: average over a vertical section $L1$ ($y = 0.2$); third column ϵ_{L2}: average over a vertical section $L2$ ($y = 0.8$). Minimum values are placed in boxes based on mask size and presented in **bold** if using a 3 × 3 mask or *italics* for a 5 × 5 mask.

DOI: 10.1002/cnm

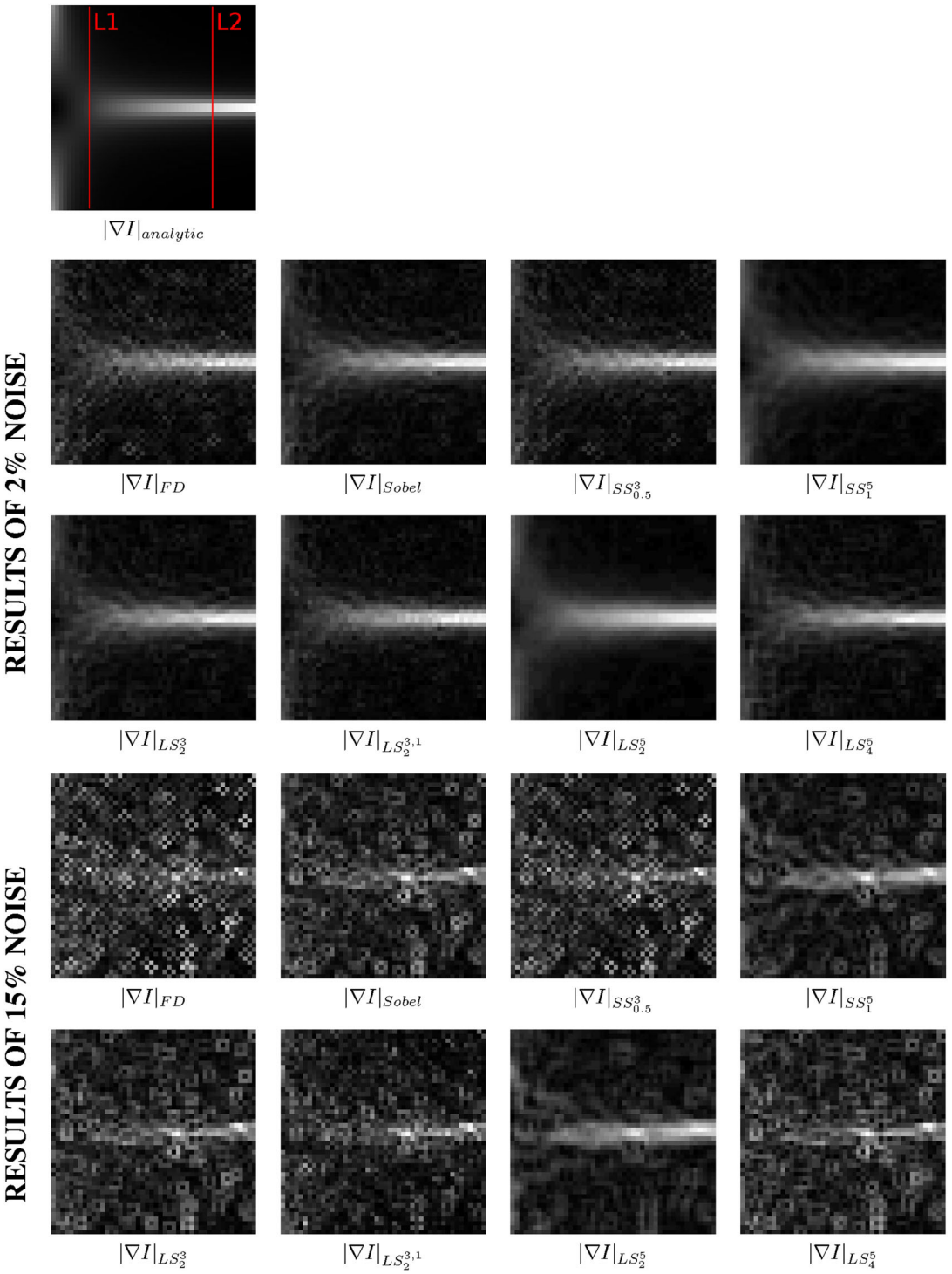

Figure 3. Gradient magnitude of the *arctan image*, computed using different approaches as discussed in Section 3. Top row: analytic solution of the image gradient magnitude; rows 2–3: results for image with 2% noise; rows 4–5: results for image with 15% noise.

DOI: 10.1002/cnm

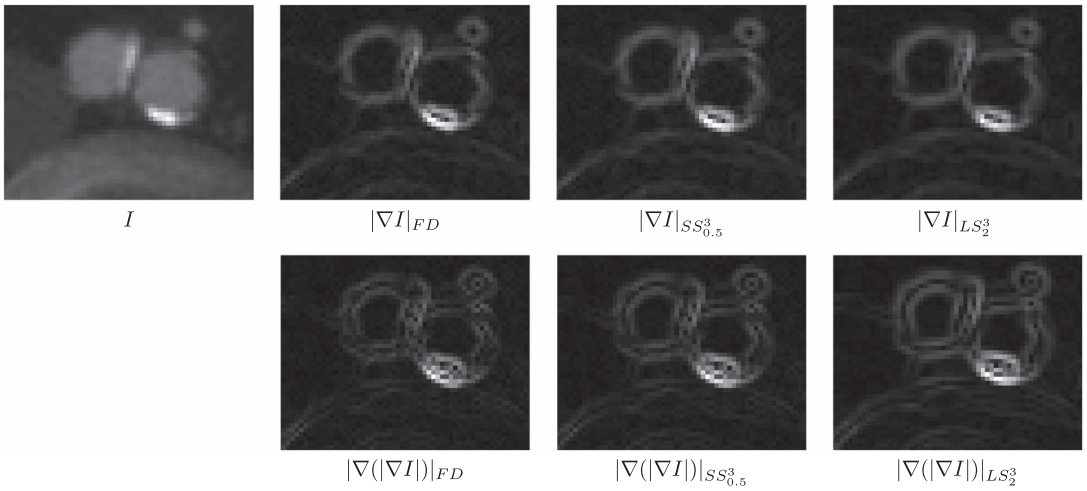

Figure 4. Comparison of the effectiveness of calculating spatial derivatives, using the *abdominal computed tomography angiography image* test case. Results for $|\nabla(|\nabla I|)|$ are obtained by initially computing $|\nabla I|$. LS^3_2 method proves to have smoother results.

Having observed results of a synthetic *arctan image*, we now observe the results on the *abdominal CTA image*, shown in Figure 4. In this case, we maintain a small mask size of 3×3 because some features present are of the order of a couple of pixels. The results for the gradient magnitude appear similar if not observed closely. A greater difference is noted when $|\nabla(|\nabla I|)|$ is computed, that is, the gradient magnitude of the gradient magnitude, computed in two steps. By repeating the process of computing the gradient in this manner, the loss of accuracy is more evident (loss of smoothness), with the LS approach performing best. We note that in practice, the second-order derivatives using the LS method are not computed in this manner but directly from equation (10).

To summarise, it has also been shown that maintaining a small sample set restricted to a 3×3 mask size, and allowing for the identification and subsequent removal of outliers (due to noise) from the data set, can improve the accuracy of the computed derivatives. This aspect becomes very important when analysing images with limited pixel resolution and the presence of noise.

Overall, the LS approach yields superior results, both in the noise-free and corrupted cases. An additional benefit of the LS method is that higher-order derivatives can be obtained effortlessly. The LS method hence proves to be accurate, easily extensible and flexible. For the remainder of the results presented in this work, the LS approach $|\nabla I|_{LS^{3,1}_2}$, hence using 3×3 mask size and excluding one outlier, will be used unless otherwise specified.

4. DENOISING FILTERS

Filtering noise is one of the most important and common medical image processing steps, and various approaches have been proposed. In order to provide a comparison of the novel tools developed in this work with existing approaches for image denoising, a brief outline is given here.

Medical imaging noise is perceived as the localised (individual pixel or small cluster of pixels) alteration in the image intensity, and is hence associated to high frequency, or equivalently to non-smooth image intensity variation and hence spurious high gradients and direction. Effective image denoising should attenuate these spurious gradients while retaining faithfully the gradients that represent the edges of anatomical objects of interest. Several approaches of filtering have been proposed in the literature [6]; however, some of the greatest success has been with PDE-based methods that rely on the diffusion equation. These methods achieve good results and are flexible to more sophisticated mathematical modelling, and the mathematical properties have been extensively investigated.

DOI: 10.1002/cnm

The simplest approach involves solving for the isotropic diffusion equation, resulting in a convolution of the Gaussian function with the image (Appendix). The result is, however, to blur both noise and desired features indiscriminately [35]. A more sophisticated approach is to use a spatially (and directionally) anisotropic diffusion coefficient [13–16, 22, 32, 40, 41]. In the work of [13], commonly referred to in the literature as the *Perona–Malik* (PM) method, the diffusion coefficient is a function of the image gradient, and the equations are given by

$$\frac{dI}{dt} = \mathrm{div}(c\nabla I) \quad ; \quad c = \frac{1}{1 + \left(\frac{|\nabla I|}{\beta}\right)^2} \tag{12}$$

where $I = I(x, y, t)$ is our grey-scale image and $c = c(x, y, t)$ is the diffusion coefficient. The problem is known to be ill-posed, and regularisation methods have been put forward with varied success and discussed in [14, 40, 41]. The PM method works by reducing the diffusion across object edges, which are identified as regions of higher gradient magnitude, while still attenuating oscillations in more uniform regions. This method has been tested for comparison purposes in this work and is abbreviated to 'PM', using freely available implementation [42].

Another proposed choice of the diffusion coefficient is for it to be a function of the Laplacian of the image [16]:

$$c = \frac{1}{1 + \left(\frac{|\Delta I|}{\beta}\right)^2} \tag{13}$$

and the regularisation of the method has been proposed in [15], where it has been termed the nonlinear complex diffusion filter (NCDF). Similarly to the PM method, diffusion across object edges is reduced; however now, the indicator is the Laplacian of the image intensity, which is related to inflexion points. This method has also been tested for comparison purposes in this work and is abbreviated to 'NCDF', using freely available implementation [43].

The above two approaches of anisotropic filtering allow the diffusion coefficient to vary spatially in order to avoid excessive blurring of desired object edges, using the image gradient magnitude and Laplacian as indicators of object boundaries. We note in passing that directional anisotropy is also possible, using a spatially varying diffusion tensor instead of a scalar [22].

These methods require a priori choice of the parameter β (as well as other regularisation parameters [15, 41]). The total integration time may be set at runtime by evaluating the mean local variance in the image. The local variance is defined as the variance of the image intensity at a given pixel, using a local computational mask, for example, a 3×3 block. In Figure 5, the mean local variance

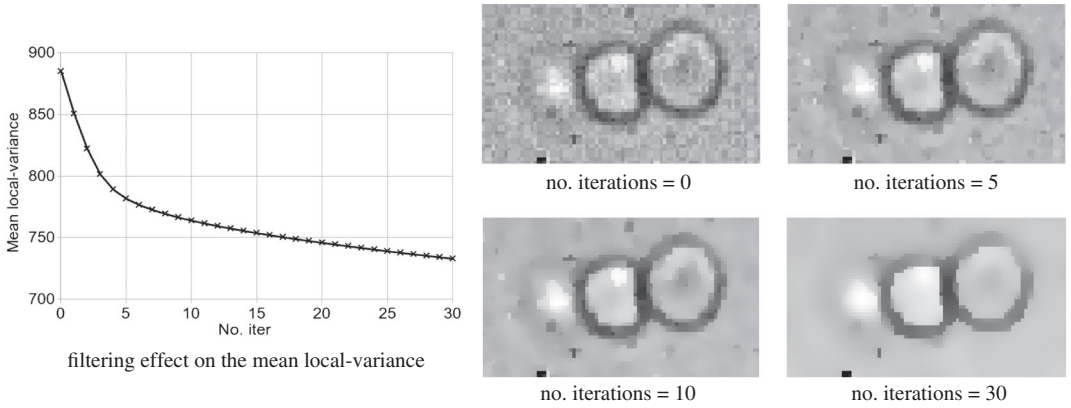

Figure 5. Results of filtering the *microscopy image* test case using the Perona–Malik method (equation (12)). The mean local variance is seen to decrease rapidly until approximately five iterations and then continue decreasing at a different rate. The optimal filtering is at the end of the initial stage, hence around five iterations. Here, $\beta = 10$ and the integration time step is $dt = 1/7$.

DOI: 10.1002/cnm

is plotted with respect to the time integration count, for the *microscopy image* test case. As the diffusion process proceeds, the first stage involves attenuating both noise and blurring object edges, while in the second stage, the noise will have been reduced sufficiently that only object edges will be blurred. Here, we assume that the noise intensity is less than the features in the image. We therefore expect two sufficiently distinct rates of decrease in the image mean local variance, as clearly seen in Figure 5. The optimal point of terminating the diffusion process is therefore the onset of the second stage, and this criterion has been used in the results section for comparison purposes.

5. PROPOSED NEW IMAGE PROCESSING SCHEME

As noted above, we investigate an approach to directly process the image intensity gradient field, as opposed to many traditional approaches that consider the image itself. Another work that employs processing of the gradient field is [19], where 'enhancement' and 'restoration' approaches are proposed. Their work utilises the structure tensor [22] for the processing, and a comparison with the 'enhancement' approach is provided in the results Section 6 and denoted by ${}_{ST}I$. The new approach developed in this section is denoted by ${}_{new}I$.

The advantages to processing the gradient field are threefold. Firstly, the information regarding object edges is readily available and can be carefully preserved: ridges in the gradient magnitude (hence first-order derivatives) and inflexion lines (hence second-order derivatives). Note that similar information is used in the anisotropic filtering methods discussed above. Secondly, object contrasts can be enhanced by directly changing the gradient field. Thirdly, noise is more evident by the differentiation process, making its identification and attenuation a simpler task.

In order to process the gradient field, we first specify what we wish to achieve and the methods employed:

- Enhance gradients: use a transfer function $E(x, y)$.
- Noise reduction: use local coherence of gradient field $N(x, y)$.
- Thin object contours: use inflexion lines as the topographic primal sketch $T(x, y)$.

Each process will produce a value for each pixel, resulting in operator images. The modified gradient field can be written as the Hadamard product of these operator images with the gradient field:

$$\nabla J_{x,y} = \nabla I_{x,y} \circ (E \circ N \circ T) \tag{14}$$

Note that the process is performed individually on the components of the gradient field and not the magnitude.

The aim is to drastically alter the image gradient and subsequently reconstruct a strikingly improved image that benefits from the aforementioned properties. The intensity of the alterations to the gradient field will be smoothed out when the integration is performed to reconstruct an image, so the approach is quite forgiving and globally insensitive to local detail. Here, some simple examples of the above three operators are presented in order to show the scope of such image processing methodology and emphasise key features. It is expected that more sophisticated approaches will yield superior results and can be tuned for different applications. In contrast, the work of [19] uses a single function (with various coefficients) to perform the processing, based on the structure tensor and the SS approach for calculating derivatives.

In order to illustrate the effect of the above operators, the modified gradient field of the *abdominal CTA image* is shown in Figure 6. It is clear that the processing of the gradient field has been striking, while the result on the reconstructed image shown in Figure 12 are encouraging.

5.1. Enhance gradients: $E(x, y)$

In order to enhance the contrast of the image, the gradients that arise at object boundaries need to be enhanced. A simple transfer function is used, given by a quarter-circle arch of radius $R = \max|\nabla I|$, hence,

$$|\nabla I(x, y)|' = \sqrt{R^2 - (R - |\nabla I(x, y)|)^2} \tag{15}$$

DOI: 10.1002/cnm

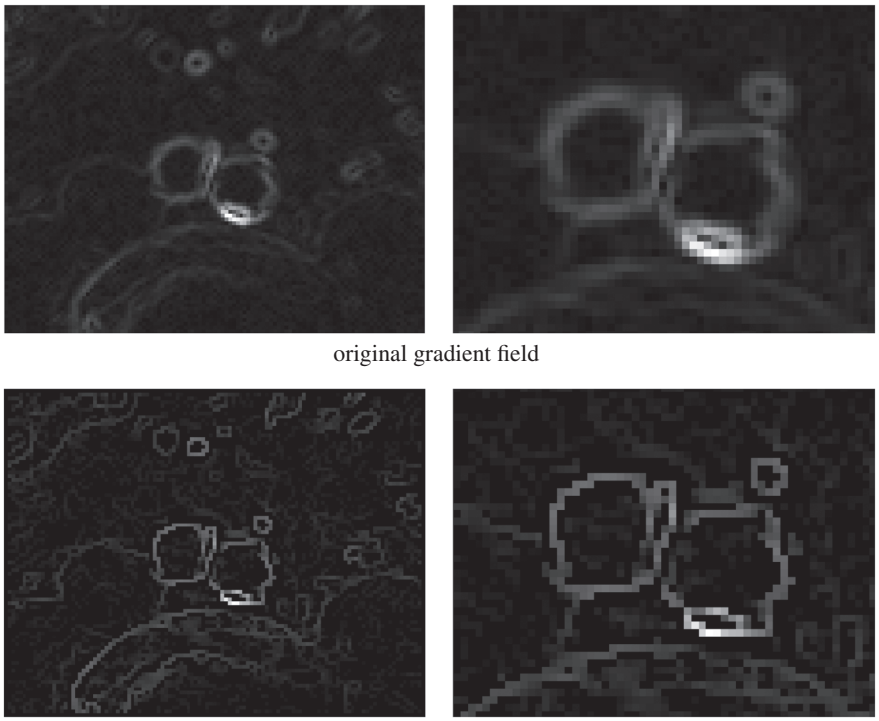

Figure 6. Gradient magnitude of the *abdominal computed tomography angiography image*. Top row: original; bottom row: modified using equation (14). Right column shows detail of the image. The processing on the gradient field can be seen to be drastic. The reconstructed image is shown in Figure 12.

The function is bounded, in other words, the enhanced image gradient will not be greater than the current maximum value. Another property of this transfer function is that the smaller values are enhanced more than the higher ones, in this way improving the dynamic range of the image. This transfer function is similar to that in [44], with the important difference that here, smaller gradients are enhanced monotonically with decreasing magnitude, and the cut-off value results in complete attenuation.

A cut-off value ω_E avoids the enhancement of irrelevant features. The resulting function for the enhancement in equation (14) is given by

$$E(x,y) = \kappa \left(\frac{|\nabla I(x,y)|'}{|\nabla I(x,y)|} \right) \qquad \text{for } |\nabla I(x,y)| > \omega_E;\ E(x,y) = 0 \text{ otherwise} \tag{16}$$

where $0 < \kappa \leqslant 1$ may be used to influence the amount of enhancing performed. In this work, $\kappa = 1$ and $\omega_E = 0.2 \max(|\nabla I|)$.

5.2. *Noise reduction:* $N(x, y)$

The level of noise can be identified in the image gradient field as local disturbances. The differentiation process emphasises the presence of noise, facilitating therefore its identification and attenuation. Several approaches can be used to suppress the noise and amongst these, the aforementioned anisotropic diffusion filters or the '*coherence*' measure using the structure tensor [19]. In order to present the approach more clearly and avoid details as to which method performs best, a simple method for noise reduction is used instead.

Here, the average dot product of the gradient vector at a pixel with its surrounding neighbours on a 3×3 mask is used. The resulting function for noise reduction in equation (14) is given by

DOI: 10.1002/cnm

$$N(x,y) = \frac{1}{8}\sum_{i=2}^{9}\left|\frac{\nabla I_1}{|\nabla I_1|}\cdot\frac{\nabla I_i}{|\nabla I_i|}\right| \qquad \text{for } N(x,y) > \omega_N;\ N(x,y) = 0 \text{ otherwise} \tag{17}$$

where $i = 1$ is the central pixel and $i = 2,\ldots,9$ are the surrounding closest neighbours. The range of values is $0 \leqslant N \leqslant 1$, with small values if noise is present and $N = 1$ in a uniform vector field. We introduce a truncation value, ω_N, in order to remove regions of highly fluctuating gradient field. In this work, we choose $\omega_N = 0.6$ and note that this value is rather insensitive to the final outcome if approximately $N(x,y) \leqslant 0.7$, while above this indicative value features in the image may be erroneously removed (depending on the smoothness of the object edge).

5.3. Thin object contours: $T(x,y)$

The thinning of object contours has several benefits, amongst which the reduction of perceived blurring that can occur when objects are out of focus or caused by imaging partial volume effects. Other benefits include easier visual distinction of object boundaries and improve robustness of subsequent gradient-based image segmentation methods. The thinning of object contours can be obtained simply from the derivative information already calculated. Here, we use a topographic representation of the image, and the object contours are the topographic primal sketch. In specific, we seek the ridges of image intensity gradient magnitude $|\nabla I|$ or inflexion lines [20].

In order to calculate these, we first compute the eigenvalues $\lambda_{1,2}$ and (unit) eigenvectors $\xi_{1,2}$ of the Hessian matrix $\mathbf{H}$, with $|\lambda_1| \geqslant |\lambda_2|$. Using this information, ridge and inflexion points can be identified as follows. A ridge point must satisfy one of the following conditions:

- $|\nabla I| \neq 0, \quad \lambda_1 < 0, \quad \nabla I \cdot \xi_1 = 0$
- $|\nabla I| \neq 0, \quad \lambda_2 < 0, \quad \nabla I \cdot \xi_2 = 0$
- $|\nabla I| = 0, \quad \lambda_1 < 0, \quad \lambda_2 = 0$

A point of inflexion is defined by the zero-crossing of the second derivatives taken in the direction of the gradient and must satisfy the following condition:

$$\tilde{\mathbf{n}}^T\mathbf{H}\,\tilde{\mathbf{n}} = 0 \qquad \text{where} \quad \tilde{\mathbf{n}} = \frac{\nabla I}{|\nabla I|} = \begin{pmatrix}\tilde{n}_x\\ \tilde{n}_y\end{pmatrix} \tag{18}$$

where $\tilde{\mathbf{n}}$ is the unit normal vector to the iso-contour. In this work, the criterion for a point of inflexion is considered, because it requires a single condition. In order to thin the gradient field, a pixel that contains a point of inflexion is given $T(x,y) = 1$ and $T(x,y) = 0$ otherwise. This binary function is used to thin and preserve object contours in equation (14).

Inflexion contours can be easily computed as the zero iso-contour of equation (18) for an image, and results are shown in Figures 11 and 13. These effectively identify object edges and hence help preserve object boundaries during the processing. We note that the criterion in equation (18) is excellent for image segmentation, and in fact, we can trivially extend the point of inflexion criterion to three dimension (3D) for object segmentation from a stack of images. Results of extracting the $\tilde{\mathbf{n}}^T\mathbf{H}\,\tilde{\mathbf{n}} = 0$ iso-surface for unprocessed *abdominal CTA image* data set in 3D are shown in Figure 7. Here, the LS_2^3 approach is used to accurately calculate the derivatives for a small mask size, by writing equation (10) to include all three Cartesian directions. This approach can be useful for direct 3D object segmentation.

5.4. Reconstructing an image from the modified gradient field

The property $\nabla \times (\nabla I) = 0$ no longer holds in the case of the modified gradient field. The result of violating this 'zero-curl' property is that the image to be reconstructed is not unique and depends on the line integral path used. A similar problem is commonly known as 'shape-from-shading', where a depth field is reconstructed from images [19, 45–49]. In [45, 46], a brief survey of existing methods is presented, together with an extremely efficient approach based on the Silvester equations, for which a freely available implementation can be found in [50]. Despite the efficiency and versatility of their method, their use of centred FD schemes results in spurious oscillations, as a chequerboard

DOI: 10.1002/cnm

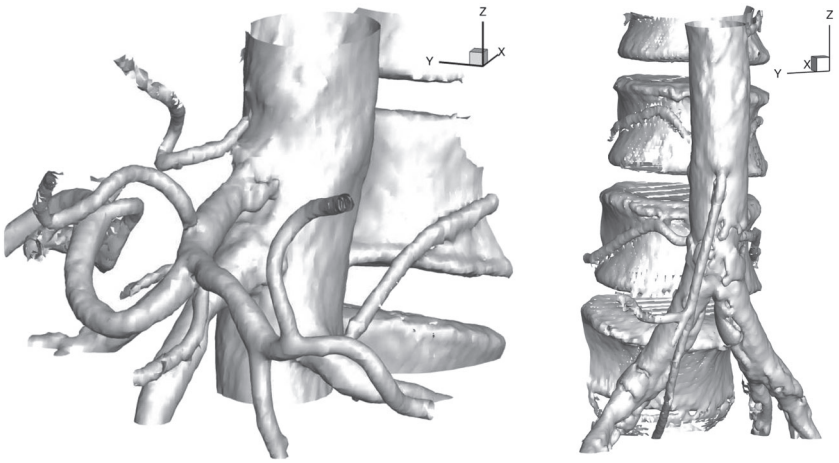

aorto-mesenteric bifurcation aorto-iliac bifurcation

Figure 7. Extracting the zero-level iso-surface of the inflexion point criterion (three-dimensional extension to equation (18)) for the descending aorta computed tomography angiography data set (unprocessed). Note that aorta and iliac arteries have nodular irregularities that correspond to atherosclerotic plaque. For clearer visibility, surrounding structures as well as features with $|\nabla I| < 3$ (units: normalised intensity per unit pixel) are removed (in an automated process with minimal user intervention).

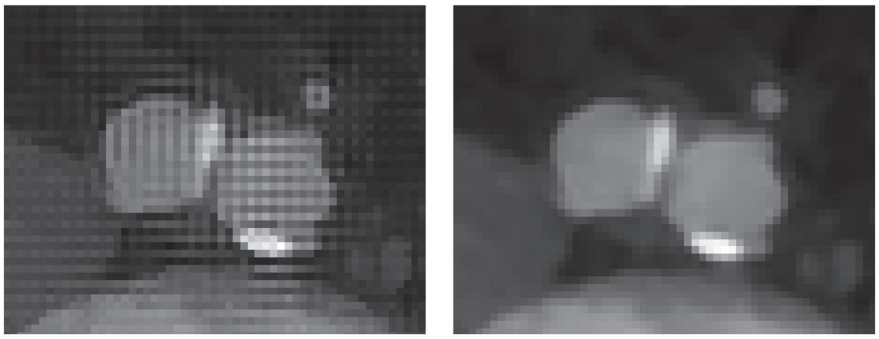

centred 2^{nd} order mixed order (2^{nd} and 1^{st})

Figure 8. Reconstruction of the image from the modified gradient field can lead to spurious oscillations (chequerboard) with a centred finite difference scheme (left). A least squares minimisation and mixed order (here, both second and first orders) lead to satisfactory results (right).

effect as seen in Figure 8. In order to solve this problem, a rather simple approach is used, relying on an LS minimisation and a mix of FD schemes. While simple, the method works well; however, it is computationally expensive and has low-order discretisation accuracy.

Let us write a global FD operator as the matrix H, which holds the FD coefficients for the entire image and acts on the processed image we are seeking Ψ. Because the image cannot be reconstructed directly as it is not unique, the problem can be solved in an LS sense.

$$\Psi = \left(H^T H\right)^{-1} H^T \nabla J \tag{19}$$

If the operator is constructed using a second-order centred scheme (as in the FD approach, see Appendix), a chequerboard effect is obtained. The matrix H is therefore simply augmented (adding extra rows) by a first-order scheme, resulting in an overdetermined linear system. Matrix H would thus have dimensions $2N \times N$, where N is the total number of pixels. The result of using this mixed-order scheme is seen in Figure 8. The mixed orders allow for a smooth solution (due to the second-order scheme) and avoid the chequerboard effect (due to the first-order scheme). Because the processed image Ψ is obtained from a least squared procedure, we find in general that $\nabla\Psi \neq \nabla J$.

DOI: 10.1002/cnm

It should be remarked that because the matrix H is sparse, the term $H^T H$ on the left hand side is not explicitly formed, and the system is solved efficiently with the conjugate gradient method, or better still with the LSQR method [51]. Finally, while this simple approach has yielded good results, it may be fruitful to use other differential operators to build H, such as those given by equation (10).

5.5. Algorithm summary

The proposed method can be summarised in the following steps:

1. Prepare the medical images: crop region of interest, apply padding and normalise the intensity.
2. Compute the spatial gradients of the image, δf, using equation (10), discarding outliers estimated by equation (11).
3. Compute the functions to enhance gradients (E), reduce noise (N), thin objects (T) and construct operator images.
4. Compute the new image gradient field, $\nabla J_{x,y}$, using equation (14).
5. Reconstruct the processed image, Ψ, using equation (19).
6. Compute the spatial gradients of image Ψ as in step 2 and extract the inflexion lines as the zero iso-surface of equation (18).

6. RESULTS

The accuracy of approximating the spatial derivatives has been presented earlier in Section 3, while here, the focus is the comparison between image processing procedures. The notation of the results is as follows: the method used to calculate the gradient is presented as before (subscript following), while the processing method used is denoted by a preceding subscript. Hence, the reconstructed image Ψ is written, for example, as ${}_{NCDF}I_{FD}$ to denote the use of the NCDF filtering approach (equation (13)) where derivatives are computed with the FD method; and ${}_{ST}I_{SS_1^5}$ denotes the Structure Tensor approach in [19] where the gradients are computed using the SS methodology (using a Gaussian function with $\sigma = 1$ and a mask size of 5×5).

Default parameters are used where possible, such that for the ${}_{NCDF}I$ method, the suggested parameters from [15] were used, for the ${}_{PM}I$ approach, $dt = 1/7$ and $\beta = 5$ (equation (12)), and for the ${}_{ST}I$ method of [19], the values of $C_{thres} = 100, \beta = 0.3, \mu = 0.5$ and $\rho = -0.3$ were used following the suggested ranges and after some testing to obtain the best results. These parameters were not changed, and the only parameter that varied was the time of diffusion in the anisotropic filtering methods, for which the stopping procedure was outlined in Section 4.

We first consider the synthetic *arctan image* with large intensity of noise, with the results shown in Figure 9. Because the original image is known, the peak signal-to-noise ratio (PSNR) and the mean structural similarity index (MSSIM) [17, 52, 53] can be used to compare both the processed images and their gradients. We note that the ${}_{NCDF}I_{FD}$ approach performs well at avoiding blurring and reducing the presence of noise; however, it is not as effective at reducing the noise as other methods. As noted above in Section 4, prolonging the diffusion process does reduce the level of noise; however, there is also an unfavourable degradation of objects by blurring. From Table I, it was shown that the Sobel approach yielded superior results with respect to $SS_{0.5}^3$ in the calculation of the gradient for the same mask size and for this reason was employed when comparing ${}_{ST}I_{Sobel}$ and ${}_{ST}I_{LS_2^{3,1}}$. We note that when considering a 3×3 mask, the latter produces better results. This indicates that because of better accuracy, the LS approach for derivative computation improves the image processing step. Both results with ${}_{ST}I$ have more blur than the result using the ${}_{NCDF}I_{FD}$ approach. We finally note that ${}_{new}I_{LS_2^{3,1}}$ reduces the noise the most while preserving the object boundary the best, both at low and high gradient regions, and does not contain significant blurring.

The PSNR and MSSIM results presented in Figure 9 indicate that the processed images have similar results, with the NCDF approach performing overall best. However, it should be stressed that the scope is not only to remove noise but also enhance the image and ensure sharp gradients. This will naturally alter the image such that it will deviate from the original; for this reason, these measures are not as high for the new method. Because it is desirable to preserve the structure of the

DOI: 10.1002/cnm

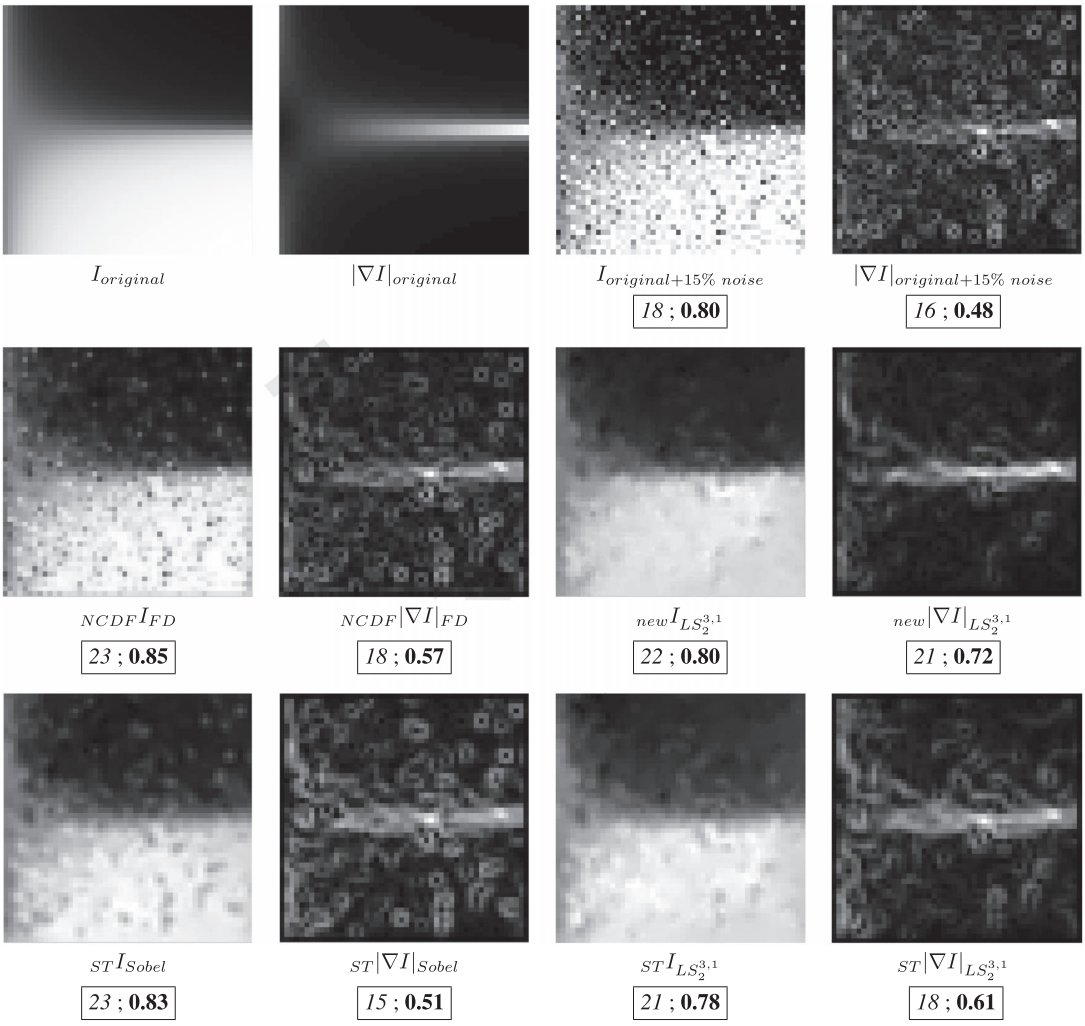

Figure 9. Results of various image processing methods, with different methods for calculating the spatial derivatives. Test image is the *arctan image* with 15% noise. Values in the boxes below each image are the peak signal-to-noise ratio (/dB) and mean structural similarity index, in *italic* and **bold,** respectively, computed by comparing the reconstructed images ($|\Psi|$) and their gradient magnitude ($|\nabla\Psi|$) with the analytic functions. Note that for comparison purposes, the Sobel method is used to compute all $|\nabla\Psi|$.

image, hence location of object edges, the measures are also computed for the normalised image gradient magnitude. From these results, the proposed method $_{new}I_{LS_2^{3,1}}$ yields the highest PSNR and MSSIM by a significant margin.

Next, we observe results of the *microscopy image*, shown in Figure 10. We note that the anisotropic filtering methods provide good noise reduction, however, not as effective as the other methods based on processing the gradient field. Once again, we note that continuing the diffusion process would not only further reduce noise but also degrade the image by blurring, hence loss of object boundary definition. The $_{ST}I$ method of [19] yields overly blurred results when using the SS approach for derivative calculation in comparison with the LS approach for the same mask size (see second row of Figure 10). We finally note that the $_{new}I_{LS}$ approach provides the best results, enhancing the visibility of the left-most red blood cell such that it can be identified reasonably. Because of significant noise in this image, the larger mask size performs best; however, we note that $_{new}I_{LS_2^{3,1}}$ outperforms $_{ST}I_{LS_2^5}$ to indicate that $_{new}I$ can yield superior results than $_{ST}I$, even for smaller mask sizes used. This is especially relevant in cases of poor spatial resolution.

DOI: 10.1002/cnm

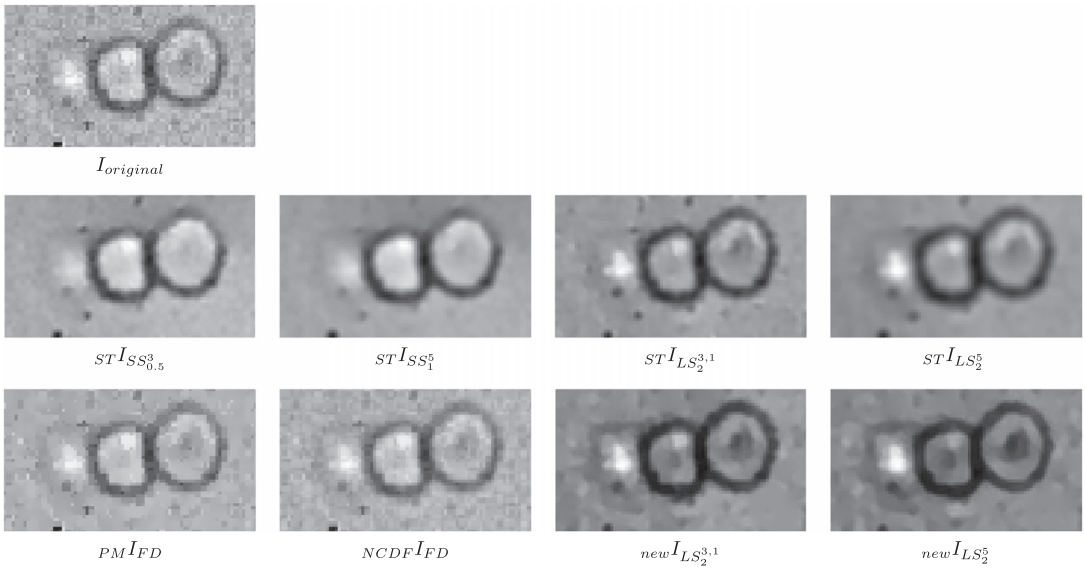

Figure 10. Results of various image processing methods, with different methods for calculating the spatial derivatives. Test image is the *microscopy image* test case, showing red blood cells.

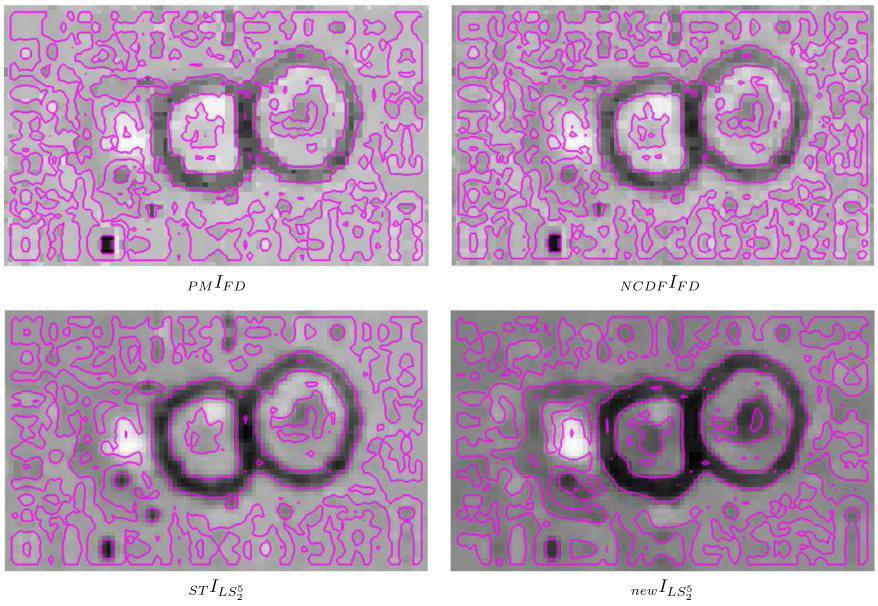

Figure 11. Results of the image processing on the *microscopy image* test. Lines of inflexion are shown (equation (18)), which were computed from the images using the LS^3_2 approach on the output image.

In order to study effects of possible segmentation of these red blood cells, we plot the inflexion lines of the processed images. These inflexion lines are the zero-crossing of the second-order derivatives taken in the direction of the gradient (Section 5.3) and are computed in this example using the LS^3_2 approach on the output image. The results are shown in Figure 11, and we note that the novel method proposed, $_{new}I_{LS^5_2}$, provides the best segmentation of the left-most red blood cell and yields the cleanest object contrast and noise attenuation.

Moving on to the *abdominal CT image*, shown in Figure 12, we note that the $_{NCDF}I_{FD}$ method provides good noise attenuation, while the object contours are minimally blurred. The results of $_{new}I_{LS^3_2}$ provide both noise attenuation and contrast enhancement, such that object contrasts are

DOI: 10.1002/cnm

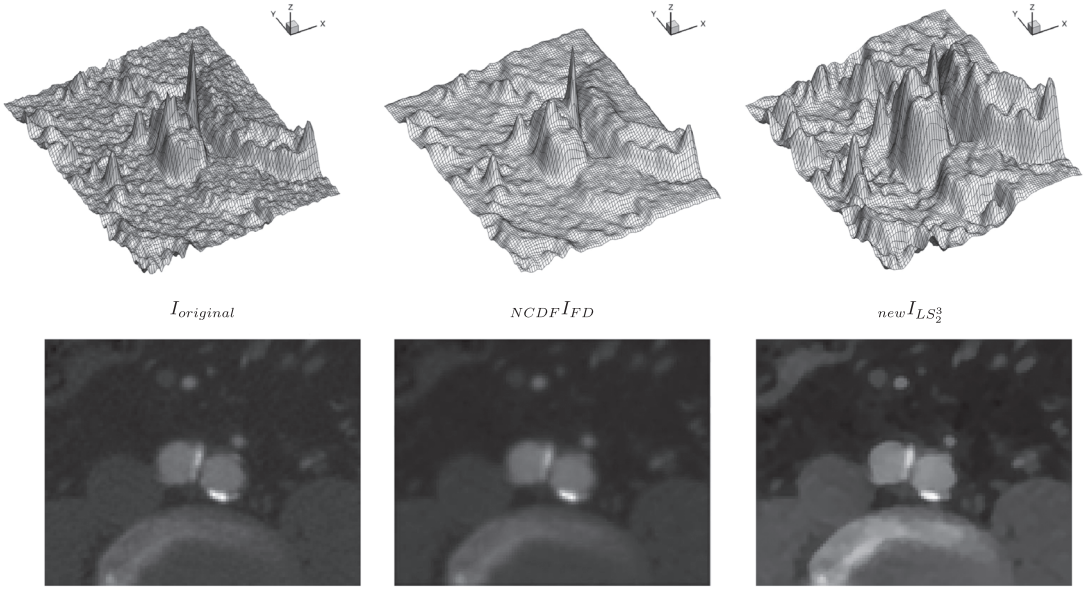

Figure 12. Results of the image processing on the *abdominal computed tomography angiography image* test. Top row shows the visualisation of the image as a topographic landscape.

emphasised, and more features in the image are now visible. We note, however, that noise has not been entirely removed, and as is common in contrast enhancement methods, the noise has also been amplified to some extent. Despite this, the resulting image is also sharper because of the thinning step in the gradient field processing, as was shown in Figure 6.

The final test performed involves the *cranial CT image*, and results are shown in Figure 13. We note from $_{ST}|\nabla I|_{SS_{0.5}^3}$ that the object boundary have been blurred, while $_{NCDF}I_{FD}$ and $_{new}I_{LS_2^{3,1}}$ provide sharper object delineation. The $_{new}I_{LS_2^{3,1}}$ method is seen to enhance features markedly in the image, which may be a desired aspect in facilitating their identification; however, this may be regulated by lowering the value of κ in equation (16). An important feature to note from these last results is that the inflexion contours no longer follow the object boundary adequately in the mid-upper region (see arrow in Figure 13) for $_{NCDF}I_{FD}$ and $_{ST}I_{SS_{0.5}^3}$, while better success is achieved with $_{new}I_{LS_2^{3,1}}$.

7. DISCUSSION

The main contributions provided by this work are twofold. Firstly, a more accurate method to compute spatial derivatives is introduced for images, based on an LS fit to the Taylor expansion and the identification of outliers, showing in general better results and especially in cases of limited resolution and the presence of noise. The second contribution is a method of processing the image gradient field directly and subsequently reconstructing the image. The results of existing methods are compared with the novel processing approaches put forward for a variety of images. The novel approach consists in three clearly distinct goals: enhance gradients, attenuate noise and thin object contour. The result is an image with improved object contrast, reduction in noise and sharper definition of objects.

The LS approach for computing the spatial derivatives gives more accurate results when compared with existing popular methods. An important benefit of using the LS approach is the possibility of maintaining high accuracy for a small computational mask size. This has meant that the use of the LS approach to calculate derivatives by itself improves the quality of results for current image processing methods. Higher-order spatial derivatives are computed effortlessly using the LS approach, allowing for extraction of inflexion lines (or surfaces) for segmenting objects. This property can be useful for preliminary object visualisation (Figure 7) or as possible initiation of level-set

DOI: 10.1002/cnm

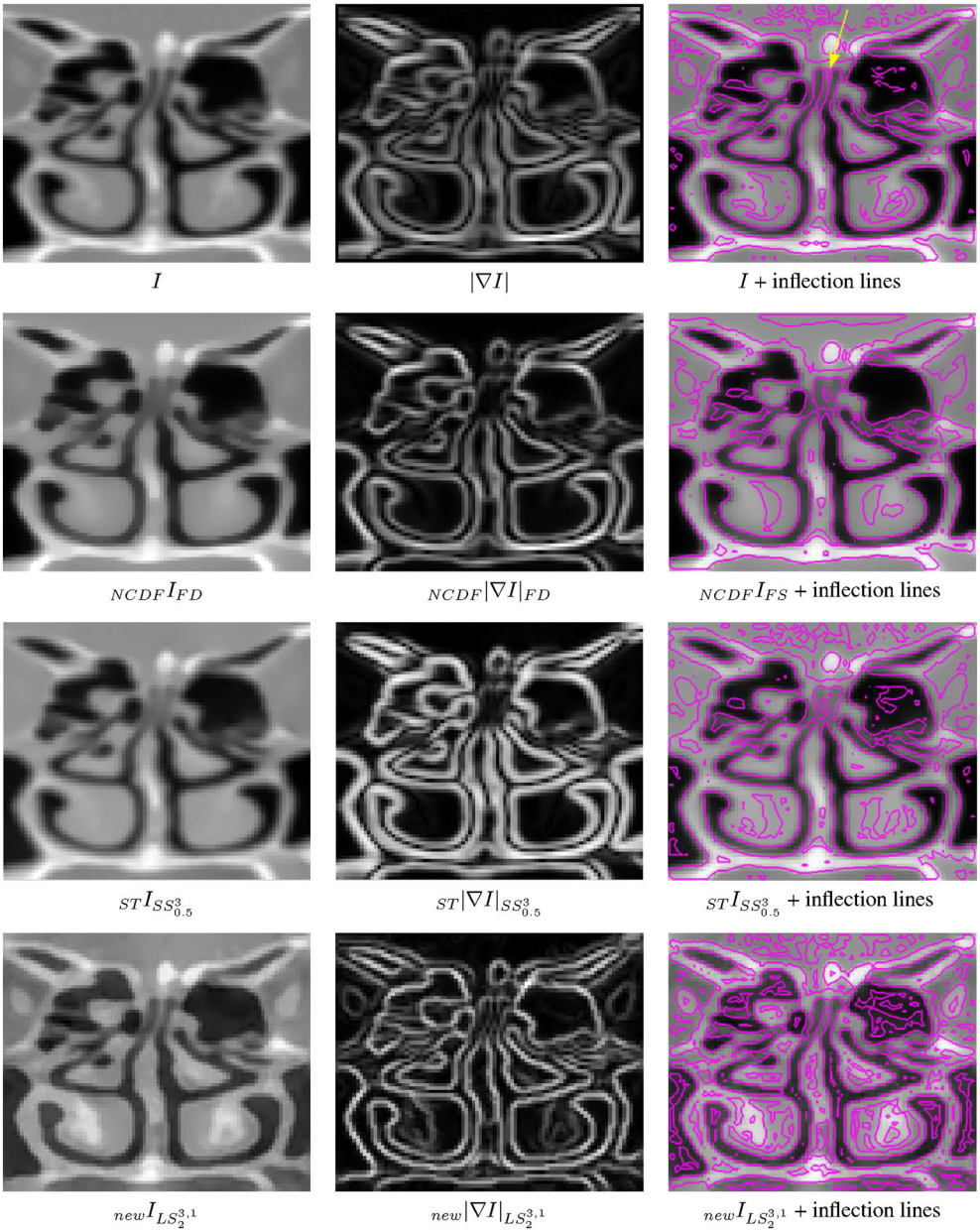

Figure 13. Results of the image processing on the *cranial computed tomography image* test. Lines of inflexion are shown (equation (18)), which were computed from the images using the LS_2^3 approach on the output image.

methods (for example, [54]). We note in passing that the work of Yeo *et al.* and Xianghua and Mirmehdi [54, 55] uses the local gradient vectors to effectively indicate the edge strength for segmenting objects, resembling similarities to the current work in the processing of the image gradient field.

The processing of the gradient field has shown to be a promising approach because the information present in the image is more readily identifiable from the spatial derivatives. The methodology discussed in this work is shown to enhance contrast and filter noise. These steps have been implemented with simple approaches, and greater success is expected if using more advanced methods. Importantly, the object boundaries are not distorted by ensuring that the contours of inflexion (the primal sketch) are unaltered. The image is then reconstructed in this work with a simple LS approach with mixed-order schemes in order to avoid chequerboard effects.

DOI: 10.1002/cnm

Overall, the procedure is shown to give good results compared with existing methods. The simple processing steps developed in Section 5 can evidently be improved; however, the goals set out give a clear indication of the important aspects to consider when performing the modifications to the gradient field. The computational time of the method is large compared with the PM and NCDF methods presented [13, 15], mostly because of solving the large linear system in equation (19). The work of [45, 46] solves this bottleneck by solving for the Sylvester equations instead; however, their implementation of the method in [50] should be developed to avoid the chequerboard effect and is beyond the scope of this work.

8. CONCLUSIONS

Medical image processing is driven by the need to identify objects and structures. Relating images to topographic landscapes, it is apparent that the underlying information of what is present in an image is given by the spatial derivatives. A novel approach is introduced to obtain improved accuracy in the computation of these derivatives, both in uncorrupted images as well as in the presence of noise and limited resolution. This approach is based on a least-squares (LS) fit to the coefficients of a Taylor expansion. The possibility of identifying outliers improves the accuracy while maintaining a small computational mask: for example, a mask of 3×3 pixels with just one outlier can provide more accurate results than existing methods in the presence of noise. Importantly, no assumption is made on the scale space (SS) of the image features, such that the image is not blurred by a convolution with a Gaussian kernel, and furthermore, no user defined parameters are necessary for small mask sizes.

Having obtained high accuracy of the spatial derivatives, the gradient field is processed directly to extract and enhance the desired features. This involves (i) reduction of noise by using a local coherence of the gradient field; (ii) enhancement of the gradient magnitude by use of a simple bounded transfer function; and (iii) thinning the gradients by using information of the inflexion points in order to preserve the location of object edges. The image is then reconstructed from the modified gradient field by using an LS approach and shows improved results with respect to existing methods. Results are presented for medical images with greatly varying characteristics: cells from confocal microscopy experiments, CTA of the aorto-iliac bifurcation and CT of the nasal cavity. These images have different levels of resolution, noise and characteristics of the objects of interest.

The results presented show the potential in exploiting the processing of the gradient field instead of the image intensity itself. It should be noted that the methods used are simple and preliminary, with much scope for further investigation and development. While the scope of the three processing steps on the image gradient field are shown to be important, there exist more sophisticated approaches for each that can lead to improved overall results. An important point to note is that a topographic interpretation has been used throughout this work; however, other approaches for edge detection (such as the Canny method) may be used in thinning the gradient field and should be explored in future work.

While the image processing was performed on individual images, extension to a 3D data set is straightforward. It has been seen that the LS reconstruction of the processed gradient field is flexible, and other processing aspects such as image restoration can easily and naturally be included in the methodology. Although segmentation has not been addressed in this work directly, it should be noted that popular methods such as level-sets use the image gradient field. The calculation of the derivatives using the LS approach as outlined in this work may therefore greatly benefit these methods. Furthermore, the image processing on the gradient field as presented in this study can evidently improve the robustness of segmentation methods, such as region-growing and level-sets, that expand and stabilise based on clear and well-defined gradients.

Improved accuracy in computing the gradient field using an LS fit to a Taylor expansion and the advantages of processing the image gradient field have been applied to medical images but are directly applicable to other image types. The simple functions to process the image gradient field outlined in Section 5 (enhance gradients, noise reduction and thin object contours) should, however, be developed to reflect the image characteristics for different applications. While these

DOI: 10.1002/cnm

simple functions have proven to work well in the case of medical images, where the object edges are smooth and the image intensity within an object does not vary significantly, they should be adapted to be more specialised in other image processing applications, such as photography.

APPENDIX A

A.1. Some popular methods for computing the derivatives

- Finite difference

  A common methodology of calculating derivatives on a structured data set is an FD scheme, such as the centred second-order accurate scheme:

$$I_x = \frac{I(x+1,y) - I(x-1,y)}{2h_x} \quad ; \quad I_y = \frac{I(x,y+1) - I(x,y-1)}{2h_y}$$

  where h_x and h_y are the pixel spacing in the x and y axes, respectively, and for simplicity, we set $h_x = h_y = 1$. This method is, however, sensitive to noise.
- Sobel operator

  An alternative discrete differential operator popular in edge detection is the Sobel operator:

$$I_x = \frac{-1}{8}\begin{bmatrix} -1 & -2 & -1 \\ 0 & 0 & 0 \\ 1 & 2 & 1 \end{bmatrix} \otimes I(x,y) \quad ; \quad I_y = \frac{-1}{8}\begin{bmatrix} -1 & 0 & 1 \\ -2 & 0 & 2 \\ -1 & 0 & 1 \end{bmatrix} \otimes I(x,y)$$

  where $\otimes$ denotes convolution. The negative sign is due to the definition of the image axes as mentioned in Section 2. The Sobel kernels can be decomposed as products of an averaging and differentiation kernels, for example,

$$\begin{bmatrix} -1 & 0 & 1 \\ -2 & 0 & 2 \\ -1 & 0 & 1 \end{bmatrix} = \begin{bmatrix} 1 \\ -2 \\ 1 \end{bmatrix} \begin{bmatrix} -1 & 0 & 1 \end{bmatrix}$$

  where the first term on the right hand side is the averaging kernel and the second term is the centred FD scheme. As a result, this method proves more reliable than the FD approach in the presence of noise. We note that the Prewitt operator is similar to the Sobel operator, but the local averaging is $[1\ 1\ 1]^T$
- Scale space

  A popular approach in image processing is to convolve the image with a Gaussian function G_σ, with standard deviation σ, and subsequently perform the derivative. This is related to the scale space [21, 31] and is understood as taking the derivatives of the image at a certain scale σ. This approach is powerful in multi-scale analysis and can improve the computations of the derivatives when noise is present in an image. The method can be written as

$$\nabla I_\sigma = \nabla (I \otimes G_\sigma) = I \otimes \nabla G_\sigma$$

  For an image, the method reverts to discretising the Gaussian function on a local mask. The result is similar to the Sobel operator approach but with the possibility of a different mask size, and the operator weights depend on the choice of the standard deviation σ. The method is therefore flexible but requires the a priori choice of σ (and subsequently the mask size).
- Savitzky–Golay

  This method uses an LS approach to fit the image intensity locally with a low-order polynomial (monomial) patch. The resulting analytic function approximating the local patch can then be differentiated analytically to obtain the spatial derivatives [23–26, 33]. We therefore seek a locally defined function $f(\mathbf{x})$ that approximates scalar values f_i at $\mathbf{x}_i$ that minimises the error functional $\epsilon = \sum_i^N |f(\mathbf{x}_i) - f_i|^2$. Locally, we can write

$$f(\mathbf{x}) = \mathbf{b}(\mathbf{x})^T \mathbf{c}$$

DOI: 10.1002/cnm

where $\mathbf{b}(\mathbf{x})$ is taken from Π_m^d, the space of polynomials of degree m in d spatial dimensions. For example, $m = 2$, $d = 2$, then $\mathbf{b}(\mathbf{x}) = [1, x, y, x^2, y^2, xy]^T$. The coefficients are obtained by solving

$$\mathbf{c} = \left(\mathbf{B}^T\mathbf{B}\right)^{-1}\mathbf{B}^T\mathbf{f} \qquad \text{where} \qquad \mathbf{B} = \begin{bmatrix} \mathbf{b}(\mathbf{x}_1)^T \\ \vdots \\ \mathbf{b}(\mathbf{x}_N)^T \end{bmatrix}$$

The size of the patches used should correspond to the degree of polynomials used and the radius of compact support from which to obtain the local data set. Note that by fixing the polynomial order and spatial dimension, the matrix $(\mathbf{B}^T\mathbf{B})^{-1}\mathbf{B}^T$ does not change and need only be computed once. In passing, we mention that other methods have been proposed using orthogonal polynomials instead of the monomial basis, showing improved results [34, 35].

A.2. Isotropic diffusion

Let us consider the homogeneous and isotropic diffusion equation

$$\frac{d\phi}{dt} = \alpha\nabla^2\phi \tag{A. 1}$$

where $\alpha > 0$ is the diffusion coefficient and ϕ is a scalar function. Let us also consider the initial condition is a point source (Dirac delta) of unit magnitude and located at the origin, then for a d-dimensional problem, the solution is given by

$$\phi(\mathbf{x}, t) = \left(\frac{1}{\sqrt{4\pi\alpha t}}\right)^d \exp\left(-\frac{r^2}{4\alpha t}\right) \tag{A. 2}$$

where r^2 denotes the distance from the origin: $r^2 = x^2 + y^2$ in the case of $d = 2$ in a Cartesian frame. It is apparent that the solution is a linear addition in the spatial dimensions. This result corresponds to a Gaussian function with normal probability distribution with mean $= 0$ and variance $\sigma^2 = 2d\alpha t$; hence, the dependence of the variance on time is linear. The Gaussian function is the Green's function, the impulse response, for the diffusion equation. The solution of the equation at later times is given by the convolution of the Gaussian function (with corresponding variance) with the initial condition. The diffusion coefficient can also be written as a tensor in order to identify directional anisotropy. In this case, the Gaussian function will not be symmetric but will have major and minor axes as defined by the tensor.

ACKNOWLEDGEMENTS

The author gratefully acknowledges support from project 'MatComPhys' under the European Research Executive Agency FP7-PEOPLE-2011-IEF framework. The medical and experimental image data are gratefully acknowledged from the following institutions: the Faculty of Medicine of the University of Lisbon and Hospital Santa Maria under the group of Prof. Jorge Campos; Prof. Rui Lima and the research team from Instituto Politécnico de Bragança, supported by FCT project BIOMIMETICPTDC/SAU-ENB/116929/2010; and Prof. Takuji Ishikawa and the research team at the Biological Flow Studies Laboratory from Tohoku University.

REFERENCES

1. Egmont-Petersen M, de Ridder D, Handels H. Image processing with neural networks: a review. *Pattern Recognition* 2002; **35**:2279–2301.
2. Lehmann TM, Gonner C, Spitzer K. Survey interpolation methods in medical image processing. *IEEE Transactions on Medical Imaging* 1999; **18**(11):1049–1075.
3. Heimann T, Meinzer H. Statistical shape models for 3D medical image segmentation: a review. *Medical Image Analysis* 2009; **13**:543–563.
4. Oliveira FPM, Tavares JMRS. Medical image registration: a review. *Computer Methods in Biomechanics and Biomedical Engineering* 2014; **17**(2):73–93.

5. Ma Z, Tavares JMRS, Jorge RN, Mascarenhas T. A review of algorithms for medical image segmentation and their applications to the female pelvic cavity. *Computer Methods in Biomechanics and Biomedical Engineering* 2010; **13**(2):235–246.
6. Buades A, Coll B, Morel J. A review of image denoising algorithms with a new one. *Multiscale Modeling & Simulation* 2005; **4**(2):490–530.
7. The application of adaptive unsharp mask algorithm in medical image enhancement. *Cross Strait Quad-Regional Radio Science and Wireless Technology Conference (CSQRWC), Harbin* 2011; **2**:26-30.
8. Polakowski WE, Cournoyer DA, Rogers SK, DeSimio MP, Ruck DW, Hoffmeister JW, Raines RA. Computer-aided breast cancer detection and diagnosis of masses using difference of Gaussians and derivative-based feature saliency. *IEEE Transactions on Medical Imaging* 1997; **16**(6):811–819.
9. Jobson DJ, Rahman Z, Woodell GA. Properties and performance of a center/surround Retinex. *IEEE Transactions on Image Processing* 1997; **6**(3):451–462.
10. Rahman Z, Jobson DJ, Woodell GA. Retinex processing for automatic image enhancement. *Journal of Electronic Imaging* 2004; **13**(1):100–110.
11. Chao W, Cho C, Shih Y, Chen Y, Chang C. Correction of inhomogeneous MR images using multiscale retinex. *International Journal of Image Processing* 2007; **1**(1):1–16.
12. Rizzi A, Gatta C, Marini D. A new algorithm for unsupervised global and local color correction. *Pattern Recognition Letters* 2003; **24**:1663–1677.
13. Perona P, Malik J. Scale-space and edge detection using anisotropic diffusion. *IEEE Transactions on Pattern Analysis and Machine Intelligence* 1990; **12**(7):629–639.
14. Guidotti P, Kim Y, Lambers J. Image restoration with a new class of forward-backward-forward diffusion equations of Perona–Malik type with applications to satellite image enhancement. *SIAM Journal on Imaging Sciences* 2013; **6**(3):1416–1444.
15. Bernardes R, Maduro C, Serranho P, Araújo A, Barbeiro S, Cunha-Vaz J. Improved adaptive complex diffusion despeckling filter. *Optical Express* 2010; **18**(23):24048–24059.
16. Gilboa G, Sochen N, Zeevi YY. Image enhancement and denoising by complex diffusion processes. *IEEE Transactions on Pattern Analysis and Machine Intelligence* 2004; **26**(8):1020–1036.
17. Wang Z, Bovik AC, Sheikh HR, Simoncelli EP. Image quality assessment: from error visibility to structural similarity. *IEEE Transactions on Image Processing* 2004; **13**(4):600–612.
18. Yang S, Tai S. Fast and reliable image-noise estimation using a hybrid approach. *Journal of Electronic Imaging* 2010; **19**(3):033007-033007.
19. Wang H, Chen Y, Fang T, Tyan J, Ahuja N. Gradient adaptive image restoration and enhancement. *IEEE International Conference on Image Processing*, Vol. 8-11, October 2006; 2893–2896.
20. Haralick RM, Watson LT, Laffey TJ. The topographic primal sketch. *The International Journal of Robotics Research* 1983; **2**(1):50–72.
21. Witkin AP. Scale-space filtering: a new approach to multi-scale description. *IEEE International Conference on Acoustics, Speech, and Signal Processing, ICASSP'84*, Vol. 9, San Diego, California, March 19–21, 1984.
22. Weickert J. Scale-space properties of nonlinear diffusion filtering with a diffusion tensor. *Technical Report No. 110*, Laboratory of Technomathematics, University of Kaiserslautern, 1994.
23. Savitzky A, Golay MJE. Smoothing and differentiation of data by simplified least squares procedures. *Analytical Chemistry* 1964; **36**(8):1627–1639.
24. Chinrungrueng C, Suvichakorn A. Fast edge-preserving noise reduction for ultrasound images. *IEEE Transactions on Nuclear Science* 2001; **48**(3):849–854.
25. Luo J, Ying K, He P, Bai J. Properties of Savitzky-Golay digital differentiators. *Digital Signal Processing* 2005; **15**:122–136.
26. Schafer RW. What is a Savitzky-Golay filter. *IEEE Signal processing Magazine* 2011; **28**(4):111–117.
27. Liszka T, Orkisz J. The finite difference method at arbitrary irregular grids and its application in applied mechanics. *Computers and structures* 1980; **11**:83–95.
28. Liszka TJ, Duarte CAM, Tworzydlo WW. hp-Meshless cloud method. *Computer Methods in Applied Mechanics and Engineering* 1996; **139**(1):263–288.
29. Lima R, Ishikawa T, Imai Y, Takeda M, Wada S, Yamaguchi T. Measurement of individual red blood cell motions under high hematocrit conditions using a confocal micro-PTV system. *Annals of Biomedical Engineering* 2009; **37**(8):1546–1559.
30. Doorly DJ, Taylor DJ, Gambaruto AM, Schroter RC, Tolley N. Nasal architecture: form and flow. *Philosophical Transactions of the Royal Society A-Mathematical Physical and Engineering Sciences* 2008; **366**:3225–3246.
31. ter Haar Romeny BM, Florack LMJ, Salden AH, Viergever MA. Higher order differential structure of images. *Image and Vision Computing* 1994; **12**(6):317–325.
32. Weickert J. Coherence-enhancing diffusion filtering. *International Journal of Computer Vision* 1999; **31**(2–3): 111–127.
33. Van De Weijer J, Van Den Boomgaard R. Least squares and robust estimation of local image structure. *International Journal of Computer Vision* 2005; **64**(2-3):143–155.
34. Meer P, Georgescu B. Edge detection with embedded confidence. *IEEE Trans on Pattern Analysis and Machine Intelligence* 2001; **23**(12):1351–1365.
35. Weiss I. High-order differentiation filters that work. *IEEE Trans on Pattern Analysis and Machine Intelligence* 1994; **16**(7):734–739.

DOI: 10.1002/cnm

36. Meer P, Weiss I. Smoothed differentiation filters for images. *Proc. 10th International Conference on Pattern Recognition*, Atlantic City, NJ, June 16–21, 1990; 121–126.
37. Ding H, Shu C, Yeo KS, Xu D. Development of least-squares-based two-dimensional finite-difference schemes and their application to simulate natural convection in a cavity. *Computers and Fluids* 2004; **33**:137–154.
38. Kuhnert J, Tiwari S. Finite pointset method based on the projection method for simulations of incompressible Navier-Stokes equations. *Meshfree Methods for Partial Differential Equations, Lecture Notes in Computational Science and Engineering* 2003; **26**:373–387.
39. Tseng AA, Gu SX. A finite difference scheme with arbitrary mesh systems for solving high-order partial differential equations. *Computers and Structures* 1989; **31**(3):319–328.
40. Guidotti P. A backward-forward regularization of the Perona-Malik equation. *Journal of Differential Equations* 2012; **252**(4):3226–3244.
41. Guidotti P. A new well-posed nonlinear nonlocal diffusion. *Nonlinear Analysis: Theory, Methods & Applications* 2010; **72**(12):4625–4637.
42. Matlab code: "anisodiff2D.m", Lopes DS. *ICIST, Instituto Superior Técnico, UTL*, 2007. (Available from: http://www.mathworks.co.uk/matlabcentral/fileexchange/14995-anisotropic-diffusion--perona---malik-) [Accessed on 16 May 2007].
43. Matlab code: "twodncdf.m". *AIBILI – Association for Innovation and Biomedical Research on Light and Image*, 2012. (Available from: http://www.mathworks.co.uk/matlabcentral/fileexchange/29801-image-filtering) [Accessed on 9 April 2012].
44. Yu Z, Bajaj C. A fast and adaptive method for image contrast enhancement. *Proceedings of 2004 IEEE International Conference on Image Processing (ICIP'04)*, Singapore, Oct 2004; 21001-1004.
45. Harker M, O'Leary P. Least squares surface reconstruction from measured gradient fields. *IEEE Conference on Computer Vision and Pattern Recognition, CVPR 2008*, Anchorage, June 2008; 23–28.
46. Harker M, O'Leary P. Regularized reconstruction of a surface from its measured gradient field. *Journal of Mathematical Imaging and Vision* 2014:1–25.
47. Karaçali B, Snyder W. Reconstructing discontinuous surfaces from a given field using partial integrability. *Computer Vision and Image Understanding*; **92**:78–111.
48. Zhang R, Tsai P, Cryer JE, Shah M. Shape from shading: a survey. *IEEE Transactions on Pattern Analysis and Machine Intelligence* 1999; **21**(8):690–706.
49. Ng HS, Wu TP, Tang CK. Surface-from-gradients without discrete integrability enforcement: a Gaussian kernel approach. *IEEE Transactions on Pattern Analysis and Machine Intelligence* 2010; **32**(11):2085–2099.
50. Matlab code: "g2s.m", Harker M, O'Leary P, 2013. (Available from: http://www.mathworks.co.uk/matlabcentral/fileexchange/43149-surface-reconstruction-from-gradient-fields--grad2surf-version-1-0) [Accessed on 20 August 2013].
51. Paige CC, Saunders MA. LSQR: an algorithm for sparse linear equations and sparse least squares. *ACM Transactions on Mathematical Software (TOMS)* 1982; **8**(1):43–71.
52. de Araujo AF, Constantinou CE, Tavares JMRS. New artificial life model for image enhancement. *Expert Systems with Applications* 2014; **41**(13):5892–5906.
53. Matlab code: "ssim.m", Wang Z. *SSIM index with automatic downsampling, version 1.0.* (Available from: https://ece.uwaterloo.ca/z70wang/research/ssim/) [Accessed on 27 June 2009, Version: 1.0].
54. Yeo SY, Xianghua X, Sazonov I, Nithiarasu P. Geometrically induced force interaction for three-dimensional deformable models. *IEEE Transactions on Image Processing* 2011; **20**(5):1373–1387.
55. Xianghua X, Mirmehdi M. Magnetostatic field for the active contour model: a study in convergence. *Proceedings of British Machine Vision Conference*, Vol. 4-7, Edinburgh, September 2006; 127–136.

DOI: 10.1002/cnm